# Langmuir probe measurements in a dual-frequency capacitively coupled rf discharge

J. Schleitzer, <sup>1</sup> V. Schneider, <sup>1</sup> I. Korolov, <sup>2</sup> G. Hübner, <sup>2</sup> P. Hartmann, <sup>3</sup> J. Schulze, <sup>2</sup> and H. Kersten <sup>1</sup> Institute of Experimental and Applied Physics, University of Kiel, Leibnizstraße 19, 24108 Kiel, Germany.

<sup>2)</sup>Chair of Applied Electrodynamics and Plasma Technology, Faculty of Electrical Engineering and Information Sciences, Ruhr University Bochum, Universitaetsstraße 150, 44780 Bochum, Germany.

<sup>3)</sup>Institute for Solid State Physics and Optics, Wigner Research Centre for Physics, Konkoly-Thege Miklós Str. 29-33, 1121 Budapest, Hungary.

(\*Electronic mail: schleitzer@physik.uni-kiel.de)

(Dated: 1 March 2024)

A dual-frequency (2f) capacitively coupled rf argon plasma has been investigated using a passively compensated Langmuir probe. The discharge is driven by two different excitation frequencies  $(13.56\,\mathrm{MHz}$  and  $27.12\,\mathrm{MHz})$  simultaneously with a variable phase angle  $\theta$  between them, utilizing the electrical asymmetry effect (EAE). Two plasma chambers with different degrees of geometric asymmetry are subject of investigation. The qualitative trends of floating potential, plasma potential, electron temperature and electron density are measured for various phase angles between  $0^\circ - 180^\circ$  in these two reactors to conduct a cross-chamber validation of parameter trends. Similar to the dc self-bias, the plasma parameters show a pronounced dependence on the phase. Their general behavior can be explained by the phase-dependent sheath expansion dynamics as shown by PIC/MCC simulations, where beams of electrons are generated by the respective expanding sheath and accelerated into the plasma bulk, leading to phase-dependent electron temperature and density. However, the measured profiles of the plasma parameters as a function of phase in both experimental setups are not symmetric around  $\theta = 90^\circ$ , unlike the dc self-bias. This observation is confirmed by PIC/MCC simulations, which reveal asymmetrical electron excitation/ionization dynamics at the corresponding phases. This implies that the observed trends are a property of the 2f discharge in combination with a geometrically asymmetric reactor.

## I. INTRODUCTION

Capacitively coupled radio frequency plasmas (CCPs) have a wide range of applications in industry and research. For example, one important area is the surface treatment of semiconductors, where CCPs are used for etching solid surfaces<sup>1</sup>, cleaning substrates<sup>2</sup> or depositing thin layers<sup>3</sup>. Furthermore, CCPs are used in the production of solar cells<sup>4</sup>, displays<sup>5</sup> and microelectronics<sup>6</sup>, or in medicine for the production of biocompatible surfaces<sup>7</sup>. For these applications, the ion energy and ion flux at the electrode surface are essential. The energy of the ions striking the substrate affects the individual chemical or physical processes, respectively, while the ion flux determines the efficiency of a particular process<sup>8</sup>. A separate and independent control of these two parameters is highly desired, but not realizable in common single-frequency discharges. One approach for implementing this separate control is the electrical asymmetry effect (EAE) via a dual-frequency (2f) discharge<sup>8–21</sup>, where the dc self-bias, the mean sheath voltages, and, consequently, the mean ion energies at both electrodes can be controlled by adjusting the relative phase between two consecutive driving harmonics. Usually, it is operated at 13.56 MHz and 27.12 MHz with a fixed but adjustable phase angle  $\theta$  between the driving voltages.

To understand the basic physics of this particular discharge, plasma diagnostics are mandatory. Simulations were performed, which investigate the separate control of ion energy and flux<sup>8,18,22,23</sup>, the phase dependent electron heating dynamics<sup>14,24</sup> or an enhancement of the EAE through nonequal relative voltage amplitudes<sup>12</sup>. Radially resolved multipole resonance probe measurements<sup>25</sup> provided information

about the radial electron density distribution within the discharge. Phase and space resolved optical emission spectroscopy (PROES) revealed experimentally the dependence of the excitation dynamics on the phase angle<sup>8,26</sup>, verifying the simulations<sup>14,24</sup>. Investigations of the sheath by optically trapped microparticles<sup>27</sup> were performed, which provided an impression of the behavior and strength of the electric field force within the sheath region<sup>28</sup>.

An extended characterization of this 2f plasma is crucial for its optimization and improvement of its application. In this work, we focus on the diagnostic of a dual-frequency discharge at 1 Pa and 3 Pa argon gas pressure using a Langmuir probe (LP). It is capable of measuring a wide range of plasma parameters, including electron density, electron temperature, and plasma potential, leading to a comprehensive understanding of the plasma<sup>29</sup>. In particular, the dependence of these parameters on a phase variation is investigated, focusing on the qualitatively trends. The results are compared with and explained by PIC/MCC simulations<sup>30</sup>.

## II. THEORY

The idea of the dual-frequency discharge is based on the utilization of electrical asymmetries in the plasma by using a superposition of two consecutive harmonics to realize the following voltage drop across the plasma  $U_{\rm rf}(t)^9$ :

$$U_{\rm rf}(t) = U_{\rm dc} + \frac{1}{2} U_0 \left( \cos(2\pi f_{\rm rf} t + \theta) + \cos(4\pi f_{\rm rf} t) \right), \quad (1)$$

which comprises the dc self-bias  $U_{\rm dc}$ , fundamental frequency  $f_{\rm rf}=13.56$  MHz, identical amplitude  $U_0$  of both harmonics and phase angle  $\theta$ . Varying the phase changes the symmetry of the resulting signal waveform, i.e., the maximum  $U_{\rm rf,max}$  and minimum  $U_{\rm rf,min}$  of the applied voltage, so that  $U_{\rm rf,max} \neq |U_{\rm rf,min}|$ , resulting in a phase-dependent dc self-bias

$$U_{\rm dc} = \frac{U_{\rm rf,max} + \varepsilon U_{\rm rf,min}}{1 + \varepsilon} \tag{2}$$

and, thus, in the generation of the electrical asymmetry effect (EAE)<sup>9,25</sup>. The symmetry parameter

$$\varepsilon = \left| \frac{U_{\text{sg}}}{U_{\text{sp}}} \right| = \left( \frac{A_{\text{p}}}{A_{\text{g}}} \right)^{2} \frac{\bar{n}_{\text{sp}}}{\bar{n}_{\text{sg}}} \left( \frac{Q_{\text{mg}}}{Q_{\text{mp}}} \right)^{2} \frac{I_{\text{sg}}}{I_{\text{sp}}}$$
(3)

depends on the ratio of the maximum sheath voltages in front of the powered  $(U_{\rm sp})$  and grounded  $(U_{\rm sg})$  electrode<sup>22</sup> with the respective surface areas  $A_{\rm p}$ ,  $A_{\rm g}$  of the powered and grounded electrodes (here:  $A_{\rm p} \ll A_{\rm g}$ ), the mean ion densities  $\bar{n}_{\rm sp}$ ,  $\bar{n}_{\rm sg}$  in the respective sheath, the maximum charges  $Q_{\rm mp}$ ,  $Q_{\rm mg}$  in each sheath and the sheath integrals  $I_{\rm sp}$ ,  $I_{\rm sg}$ . With the help of the EAE, one can control the dc self-bias electrically even in geometrically symmetric discharges<sup>12</sup>. As a result, the electrode undergoes ion bombardment with energies depending on  $U_{\rm dc}$ , and adjustable by the phase angle  $\theta$ . The amplitude of the applied voltage remains unchanged during this process, ensuring that the ion flux stays nearly constant.

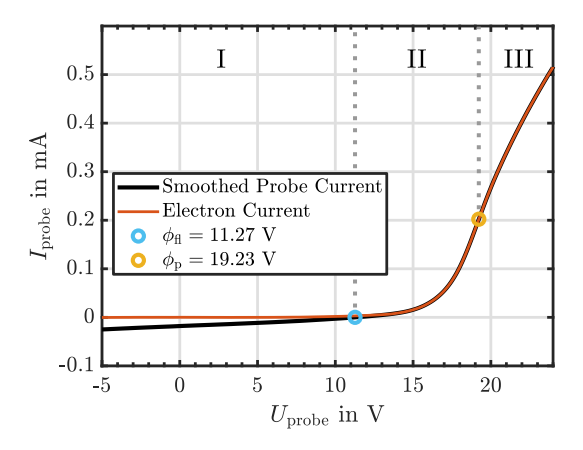
In this study, the influence of the phase on other plasma parameters is measured with a Langmuir probe. The theory of the Langmuir probe is well known and has already been described in numerous publications<sup>29,31–35</sup>, which is why only the most important aspects for the evaluation of the data are briefly given here. For the sake of simplicity, all calculations and methods presented assume the most simple case, which is collision-free with a Maxwellian electron energy distribution and one sort of single positively charged ions.

The current-voltage characteristics recorded in the 2f discharge (fig. 1 top) show three different regions: The ion saturation regime (region I), the electron retardation regime (region II) and the electron saturation regime (region III), whose limits are defined by the floating potential  $\phi_{\rm fl}$  at zero probe current and the plasma potential  $\phi_{\rm p}$ , respectively. The latter is determined by the maximum of the first derivative or zero crossing of the second derivative as shown in fig. 1 (bottom). The second derivative  ${\rm d}^2I/{\rm d}U_{\rm probe}^2$  as a function of the probe voltage shows evidence that the EEDF is close to Maxwellian, but due to the low signal-to-noise ratio, it cannot be used for accurate plasma parameter determination. The electron temperature  $T_{\rm e}$  is calculated assuming current balance<sup>35</sup> between the electron current and the ion saturation current  $I_{\rm e} = I_{\rm is}$  at  $\phi_{\rm fl}$ 

$$\frac{kT_{\rm e}}{e} = \frac{2(\phi_{\rm p} - \phi_{\rm fl})}{\ln\left(\frac{m_{\rm i}}{2\pi m_{\rm e}}\right) + 0.5},\tag{4}$$

with the mass of ions/electrons  $m_{i/e}$ , while the electron density  $n_e$  is calculated from the probe current or electron saturation current  $I_{es}$ , respectively, at plasma potential

$$n_{\rm e} = \frac{4I_{\rm es}}{A_p e \sqrt{\frac{8kT_e}{\pi m_{\rm e}}}},\tag{5}$$



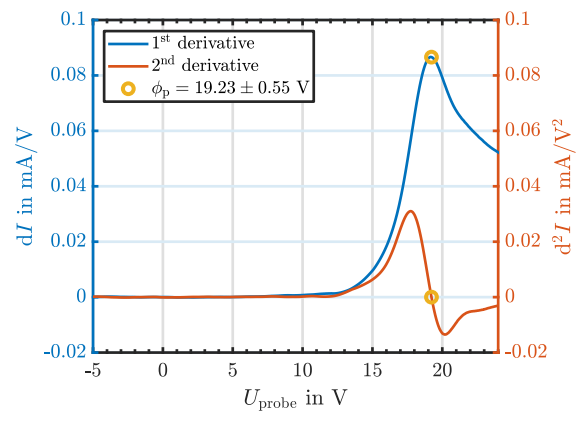


FIG. 1. Langmuir probe I-U characteristic obtained in a 2f argon discharge at 3 Pa and  $\theta = 111^{\circ}$  with a probe length of  $l_p = 6$  mm (top). First and second derivative of the probe current for the determination of the plasma potential  $\phi_D$  (bottom).

for the cylindrical probe area  $A_p = 2\pi r_p l_p$ . The ion saturation current is approximated by a straight line within the ion saturation regime and subtracted from the total probe current.

## III. EXPERIMENTAL SETUP

# A. Langmuir probe

The principle setup of the Langmuir probe (LP, fig. 2) consists of a tungsten wire as probe tip with a diameter of  $d_{\rm p}=2r_{\rm p}=100~\mu{\rm m}$  and a length of  $l_{\rm p}\approx 6~{\rm mm}$  - the rest of which is shielded with a ceramic tube - a filter system and a current/voltage measurement unit.

Since the probe is used in an rf plasma, where the plasma potential varies in the plasma bulk according to the rf frequency, it is equipped with corresponding filters to compensate for the disturbances caused by the rf signal. For this purpose, a passive compensation method is used<sup>36–39</sup>. It consists of several low-pass filters, which suppress the rf fluctuations right behind the probe, and an additional floating pick-up probe, following a probe design suggested by Godyak et al.<sup>40</sup>. It picks up the rf fluctuations and transmits them to the Lang-

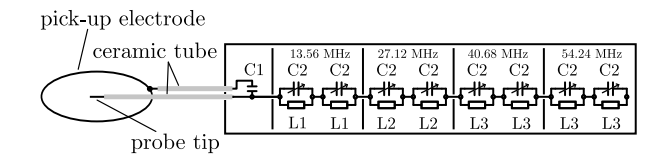


FIG. 2. RF-filter system of Langmuir probe for a 2f CCP, consisting of capacitors (C) and inductances (L). C1 = 10 pF, C2 = (4.5 - 20) pF, L1 = 10  $\mu$ H, L2 = 2.2  $\mu$ H, L3 = 1  $\mu$ H.

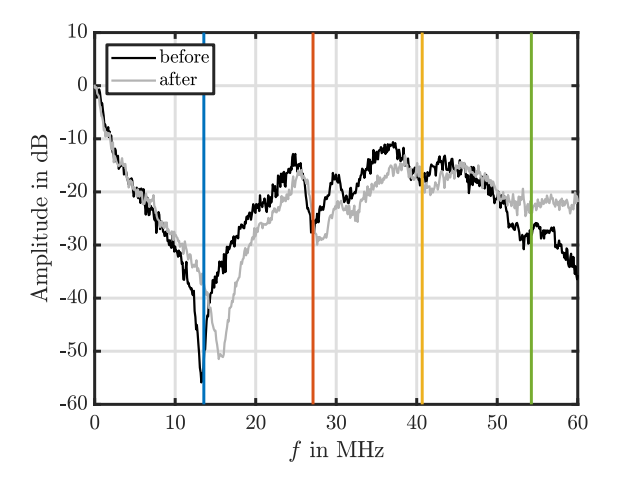
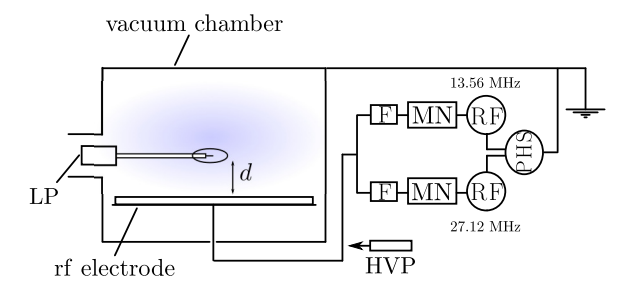


FIG. 3. Transmission spectrum of rf-filter system before the start of the measurements and after their completion several weeks later. The frequencies to be filtered are marked by the colored lines (13.56, 27.12, 40.68, 54.24) MHz. White noise was applied to the probe tip.

muir probe via a capacitor (C1 in fig. 2), that cuts off any dc current and only lets the rf pass through. This results in the probe potential being time dependent and, therefore, the probe voltage, referenced to the plasma potential, remaining stable throughout the rf cycle. The additional electrode is realized as a stainless steel wire (1 mm in diameter), which is bent to a loop with a diameter of 45 mm to not disturb the plasma in the vicinity of the probe tip but be close enough to pick up the rf near the tip.

The rf filter system comprises eight filter units, two for each 13.56 MHz-harmonic up to 54.24 MHz, inside a metal housing for proper shielding from the plasma<sup>39</sup>. The capacitors are tunable, allowing a proper calibration of the filters, which is shown in form of the transmission spectrum in fig. 3 right after the assembling of the Langmuir probe (before) and several weeks after completion of the measurements (after). The capacitors are set in such a way that maximum damping is achieved at the respective frequency. A slight difference in attenuation is noticeable between both spectra in fig. 3. There may be several reasons for this: The tungsten wire was replaced multiple times, which required opening the shielding box of the rf filter system for wire replacement. It's conceivable that this procedure may have resulted in a minor alteration in insertion loss, as no capacitor recalibration was conducted. Since capacitance is adjusted mechanically, slight variations can occur over time.



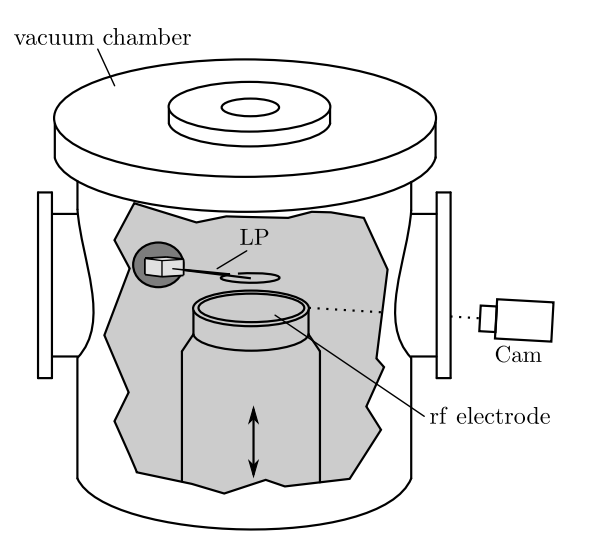


FIG. 4. Shematic of the experimental setup and the components used to generate the 2f CCP at CAU (PHS: phase shifter; RF: radio frequency generator; MN: matching network; F: filter; HVP: high voltage probe) and the Langmuir probe (LP) placement with distance d to the electrode<sup>27,28</sup>. The camera (Cam) allows taking pictures of the plasma and its sheath.

## B. Plasma chamber

The LP measurements are performed in two different plasma reactors, both of them offer the possibility of generating a 2f signal in the form of eq. 1. The first one is located at the Christian-Albrechts-University (CAU) Kiel at the Institute of Experimental and Applied Physics. The second one is at the Ruhr University Bochum (RUB) at the Chair of Applied Electrodynamics and Plasma Technology.

# 1. CAU

The experimental setup of the CCP at CAU Kiel consists of a cylindrically shaped vacuum vessel (fig. 4) with a diameter of 350 mm and a volume of 45 L, where the discharge is ignited in argon gas and operated with a frequency of 13.56 MHz and its second harmonic 27.12 MHz. The signal forms are generated in the phase shifter (PHS), amplified by the radio frequency generators (RF) and individually matched via a matching network (MN). The combined signal is coupled into the bottom electrode after passing a filter (F), which prevents power dissipation in each RF circuit by the other fre-

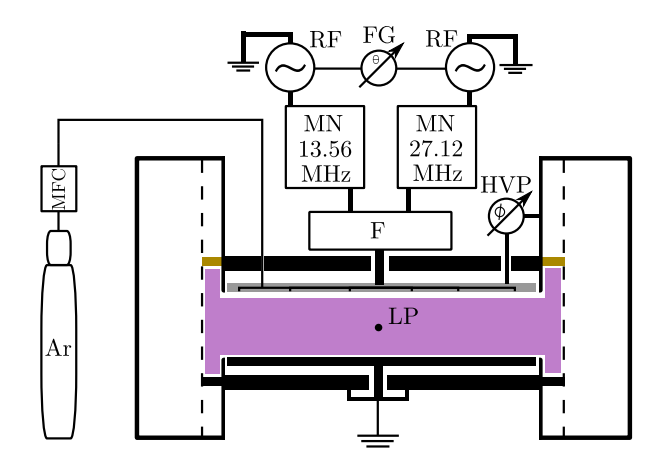


FIG. 5. Shematic of the experimental setup and the components used to generate the 2f CCP at RUB (RF: radio frequency generator; FG: function generator; MN: matching network; F: filter; HVP: high voltage probe; MFC: mass flow controller; Ar: argon gas). Adopted from Ries et al.<sup>23</sup>.

quency. The dc self-bias, signal amplitude and the phase angle between the two harmonics are monitored using a high voltage probe (HVP) and an oscilloscope. The powered electrode is water cooled, made of stainless steel and has a diameter of 100 mm. The grounded counter electrode is realized by the chamber walls, making the discharge strongly geometrically asymmetric. The Langmuir probe (LP) is introduced into the discharge through a flange of the chamber walls and centered right above the powered electrode a few millimeters away (*d*). A length of 10 cm was selected for the ceramic tube of the LP to ensure that the metal casing of the rf filter system is positioned primarily outside of the plasma. The camera (Cam) is used to take photographs of the plasma and the sheath region.

## 2. RUB

For the measurements at RUB, the experimental setup as described by Ries et al.<sup>23</sup> and shown in fig. 5 is used.

The frequencies for the capacitively coupled 2f signal (13.56 MHz and 27.12 MHz) are generated in the respective RF generator (RF) and individually matched via a matching network (MN). A bandpass filter (F) connects the matched signal to the upper electrode. The relative phase angle  $\theta$  between the two harmonics can be changed using a function generator (FG). Both the amplitude and dc self-bias of the applied signal are measured by a high voltage probe (HVP). Argon is also used here as the working gas with a continuous gas flow of 40 sccm. The electrodes have a diameter of 490 mm each with a gap of  $(75 \pm 1)$  mm between them. To confine the plasma between the electrode spacing, the electrodes are surrounded by a grounded mesh, making the grounded surface area significantly larger and, therefore, the chamber geometrically asymmetric. The upper powered electrode is made out of a mixture of aluminum and chrome, while the grounded electrode as well as the mesh are stainless steel.

The Langmuir probe (LP) is positioned in such a way that the

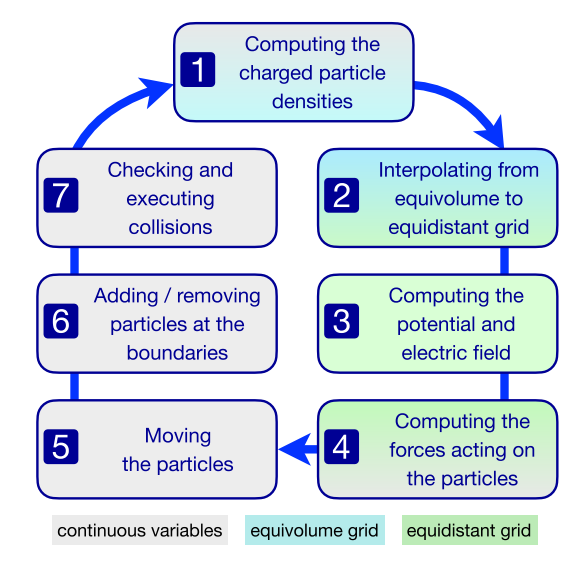


FIG. 6. Flowchart of the PIC/MCC simulation. Background colors indicate whether the step operates with continuous particle coordinates (gray), on an equivolume grid (blue), or on an equidistant grid (green), and the transitions between these options.

probe tip is horizontally and vertically in the center of the electrodes and the gap, respectively. In this system, the ceramic tube's length of the LP had to be extended to roughly 30 cm to guarantee that the metal casing remains positioned outside the shielding mesh and, thereby, outside of the plasma.

# IV. PIC/MCC SIMULATION

The model used here is based on the 2D extension of the 1D PIC/MCC code presented by Donkó et al.<sup>30</sup>. The main steps are shown in the flowchart in fig. 6. In the simulation, electrons and Ar<sup>+</sup> ions are tracked (step 5) and their collisions with the plasma facing surfaces (step 6) and background neutral Ar gas atoms at constant temperature (step 7) are considered. The collision probabilities for electrons are calculated based on the simple collision model proposed by Phelps et al.<sup>41</sup>, which reduces the collisions to three types: elastic scattering, excitation, and ionization processes. For Ar<sup>+</sup> ions – in addition to elastic, excitation, and ionization collisions the symmetric charge exchange process is also considered<sup>42</sup>. Electrostatic self-consistency is achieved by solving Poisson's equation (step 3) with the instantaneous space charge distribution and boundary conditions in each time step by implementing the parallel black-red successive over-relaxation method<sup>43</sup>. The transition between the continuous phase-space coordinates of individual particles and the spatial distributions defined on grid points (with 1024 × 1024 resolution in axial and radial directions) is realized in steps 1 and 4. The charge density distribution is first determined on an equivolume mesh, avoiding the appearance of a singularity in the center at r = 0, and later interpolated to an equidistant grid, which is used for the calculation of the electrostatic field distribution. The spatial grid and time resolutions are chosen to satisfy the

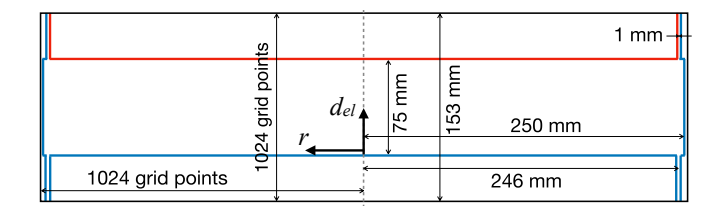


FIG. 7. Discharge geometry in the simulation. The dimensions are chosen to match the experimental plasma chamber at RUB, see fig. 5. The grounded surface is shown in blue, the powered electrode is shown in red.

general stability and accuracy criteria of the PIC/MCC numerical scheme<sup>44</sup>. Further details on the implementation of the cylindrical geometry can be found in Wang et al. 45, and on the efficient adaptation of the code to GPU architectures in Juhasz et al. 46. The simulated discharge geometry is similar to the experimental setup of the RUB chamber, with the same dimensions of the electrodes and the discharge gap, and bounded radially by the grounded grid (fig. 7). The DC selfbias voltage is found by iteratively adjusting its value, aiming at zero net conduction current at the driven electrode surface on time average. The simulation is performed for a gas pressure of 1 Pa and an amplitude of  $U_0 = 146$  V, corresponding to conditions similar to those investigated experimentally at RUB. At the planar and parallel electrodes, electrons are reflected with a probability of 50%, and the ion-induced secondary electron coefficient<sup>47</sup> is  $\gamma = 0.1$ .

A simulation based on the system at CAU was not performed due to the more complicated geometry and large reactor volume, which increases the simulation time significantly.

# V. MEASUREMENTS AND RESULTS

Before using the probe tip for measurements, it is cleaned inside the vacuum/discharge by applying a relatively low/high voltage of  $\pm 80~V$  to remove any form of unwanted residue through ion/electron bombardment<sup>48</sup>.

To maintain a constant amplitude  $U_0$  of the 2f signal, the matching settings and power of the two rf signals are modified after each phase adjustment. An additional program monitors the signal's amplitude by Fourier transforming the applied signal.

#### A. CAU

Figure 8 shows the dc self-bias  $U_{\rm dc}$  as a function of the relative phase shift of the 13.56 MHz voltage in the discharge chamber at Kiel at different pressures and an amplitude of  $U_0=187$  V. The EAE is responsible for the variation of  $U_{\rm dc}$ , which is shifted towards negative voltages due to the strong geometric asymmetry of the electrodes<sup>22,49</sup>. As predicted and shown by several simulations and measurements<sup>8–12,15,18,19</sup> the dc self-bias changes almost linearly as a function of  $\theta$  up to 90°. Its control range for the gas pressures and amplitude

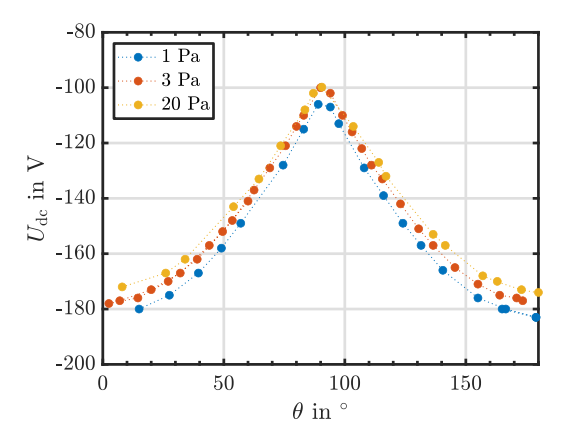


FIG. 8. Measured dc self-bias  $U_{\rm dc}$  between  $\theta=0^{\circ}$  and  $\theta=180^{\circ}$  for different pressures and  $U_0=187$  V in the chamber at CAU Kiel.

investigated is found to be close to about 42% of the applied voltage amplitude.

Similar to the dc self-bias, other plasma parameters are also influenced by a shifting phase angle. The floating potential  $\phi_{\rm fl}$ , plasma potential  $\phi_p$ , electron temperature  $kT_e$  and the electron density n<sub>e</sub> measured via Langmuir probe are presented in figure 9 for 3 Pa and  $U_0 = 187$  V. For these measurements, the probe tip was placed 17 mm above the bottom electrode. Four I-U curves were recorded and averaged per phase angle. The first three parameters (a), b), c)) show a similar trend as the dc self-bias, with the plasma potential b) and electron temperature c) indicating a slight dip at 90°.  $\phi_{\rm fl}$  exhibits a small range of control with a significant increase at 90°. The electron density d) shows a completely different behavior with a strong irregularity around 90°. It can be observed that  $\phi_p$  and especially  $kT_e$  behave contrary to the electron density, where usually an increase in  $n_e$  leads to a decrease in electron temperature due to the interplay between number of collisions and the electron energy transfer<sup>50</sup>. Consequently, the experimentally observed trend, which is the subject of investigation, aligns with the expectations.

The asymmetry in the density can already be identified from the I-U curves through the electron saturation current ( $I_{\rm es}$ ), which is the current at plasma potential. The dependence of  $I_{\rm es}$  on the phase is shown in figure 10 together with I-U curves for three different phases. Apart from the electron temperature and the probe area, the electron saturation current  $I_{\rm es}$  plays a significant role in determining the electron density (see eq. 5). From figure 10 it can be seen that the trend of  $n_{\rm e}$  is mainly determined by  $I_{\rm es}$  and that the I-U curves also have a strong dependence on the phase.

As a validation of these irregular profiles, the behavior of the light intensity of the discharge as well as the sheath extension  $d_{\rm sh}$  in front of the powered electrode while changing the phase angle were observed. Both parameters are determined using photographs of the argon discharge<sup>28</sup> (see fig. 11), providing a non-electrostatic method to analyze the plasma independent of the Langmuir probe. The position of the highest intensity of the intensity profiles (max. int.) is used as a refer-

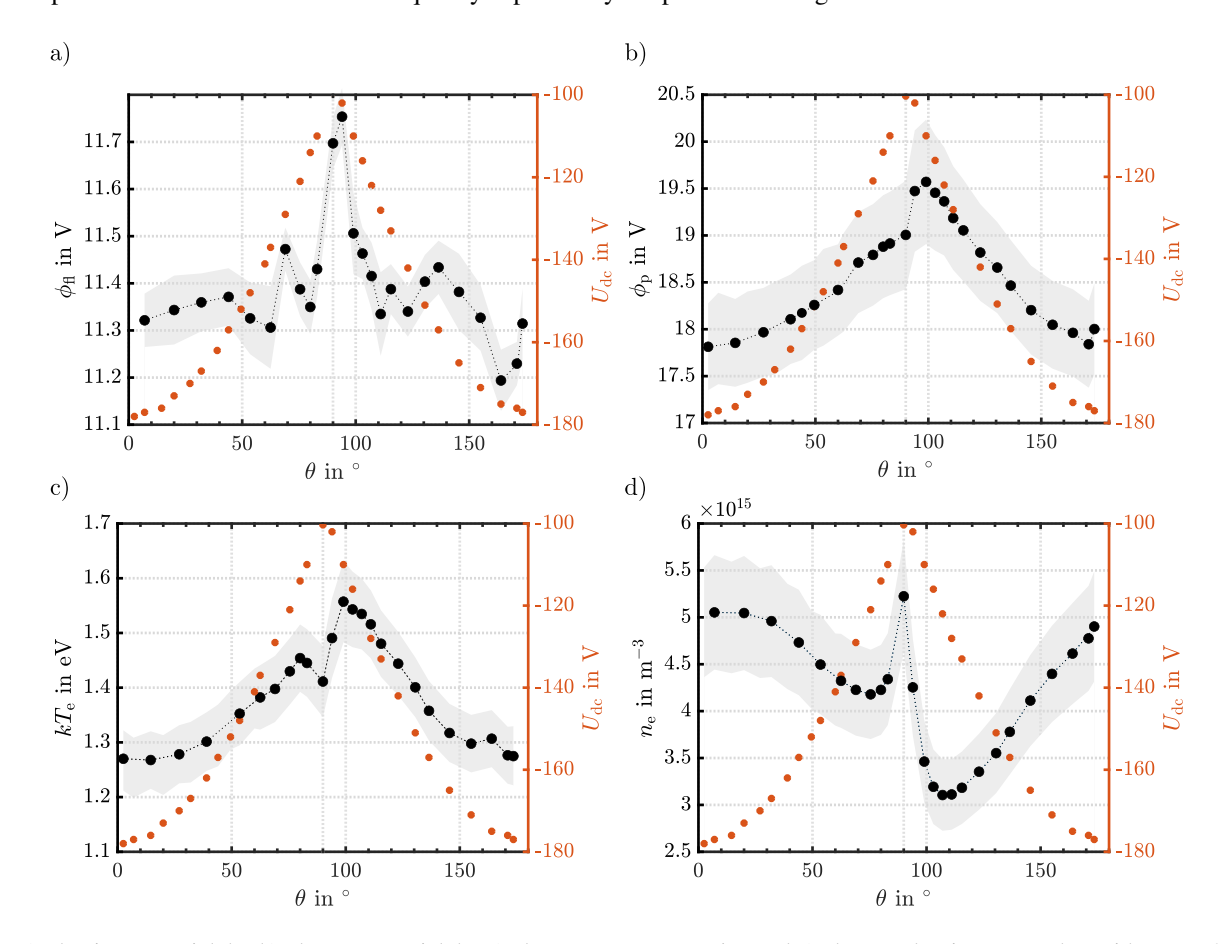


FIG. 9. a) Floating potential  $\phi_{\rm fl}$ , b) plasma potential  $\phi_{\rm p}$ , c) electron temperature  $kT_{\rm e}$  and c) electron density  $n_{\rm e}$  together with  $U_{\rm dc}$  at 3 Pa and  $U_0=187$  V. The plasma parameters were measured 17 mm above the electrode with a probe length of  $l_{\rm p}=6$  mm at CAU Kiel (fig. 4). The error margins are indicated in grey.

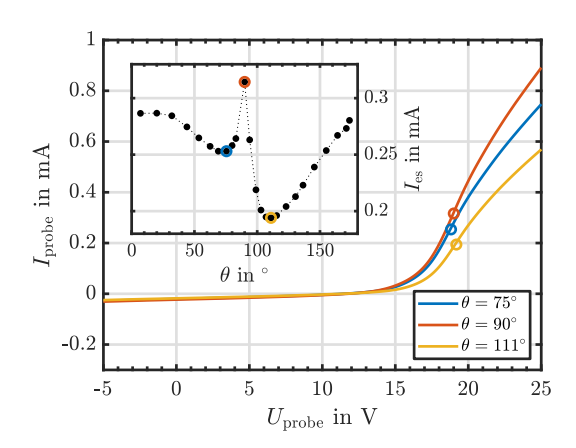


FIG. 10. I-U curves at 3 Pa and  $U_0=187$  V for three different phase angles  $\theta$ . The position of the plasma potential  $\phi_p$  or electron saturation current  $I_{\rm es}$ , respectively, for each curve is marked by a circle. The inset graph shows the dependence of  $I_{\rm es}$  on the phase.

ence for the mean sheath thickness  $d_{\rm sh}$ . A change in the phase angle  $\theta$  influences both the maximum light intensity and the mean sheath thickness, which is shown exemplarily for 3 Pa

and  $U_0 = 187$  V in fig. 12. An increase in the phase leads to an increase in the light intensity, following the asymmetric trend of the electron density (fig. 9d)), and a decrease in the sheath expansion up to  $\theta = 90^{\circ}$ . Similar to the plasma parameters, especially the electron density  $n_{\rm e}$ , an asymmetry in the sheath thickness with an extremum at  $90^{\circ}$  can be seen. According to the Child-Langmuir Law for a collisional rf sheath<sup>7</sup>, the mean thickness is proportional to

$$d_{\rm sh} \propto \left(\frac{1}{n_{\rm s}}\right)^{2/5} U_{\rm dc}^{3/5},$$
 (6)

where  $n_{\rm s}\approx 0.61n_{\rm e}$  is the plasma density at the sheath edge. These relations should serve as a rough estimate for the 2f case. A decreasing absolute value of the dc self-bias results in a decreasing sheath thickness at the powered electrode, whereby the asymmetric profile of  $d_{\rm sh}$  is following inversely the trend of the electron density, as observed experimentally in fig. 12. This measurement of the sheath thickness qualitatively confirms the measured asymmetric profiles of the plasma parameters independent of the LP.

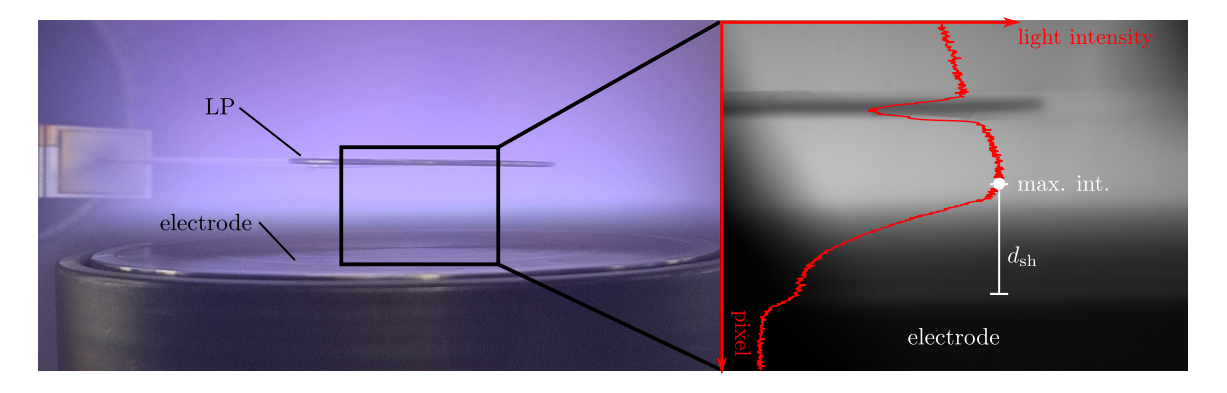


FIG. 11. Determination of mean sheath thickness  $d_{\rm sh}$  through photographs of the discharge, exemplarily shown for  $\theta = 90^{\circ}$ . An intensity profile (red curve) along the image centerline is determined for each phase, from which the maximum intensity (max. int.) and the sheath thickness are specified.

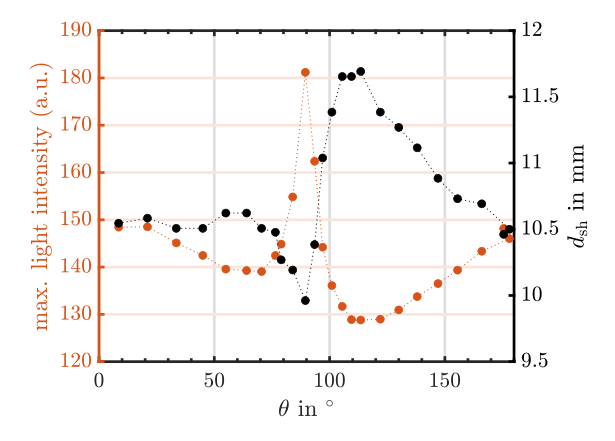
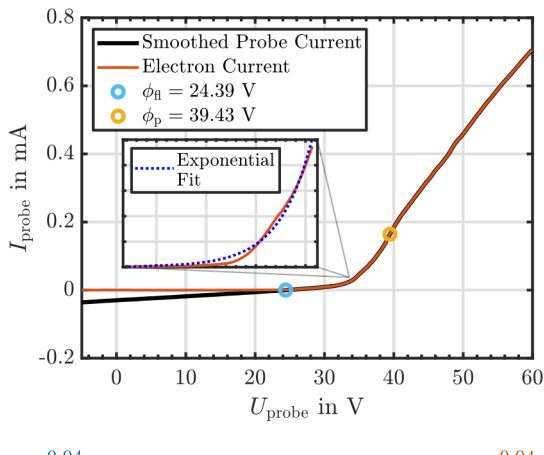


FIG. 12. Light intensity of the discharge and the sheath thickness  $d_{\rm sh}$  in front of the lower, powered electrode at 3 Pa and  $U_0=187$  V.

# B. RUB

For comparison and verification purposes, similar Langmuir probe measurements were performed in the plasma chamber at Bochum University. The aim is to investigate whether the phase asymmetry measured at CAU is a specific trait of the 2f discharge or rather an inherent characteristic of the plasma chamber itself. In figure 13, the I-U characteristic for 1 Pa,  $\theta = 60^{\circ}$  and  $U_0 = 146$  V together with the corresponding derivatives are shown. The evaluation of these curves turned out to be much more difficult due to the presence of strong noise, which has a strong impact on the derivatives (see fig. 13 bottom). The precise origin of this elevated noise level remains uncertain. It is conceivable that the noise is intensified by the extended shielding ceramic tube and tungsten wire of the LP in the RUB setup, resulting in a prolonged signal path. In this configuration, the wire also acts somewhat like an antenna. The extension of the ceramic and, consequently, the wire was necessary at RUB to position the LP's metal housing outside the surrounding mesh, thus keeping it beyond the plasma to avoid disruption.

Additionally, the curves in figure 13 indicate a slight devi-



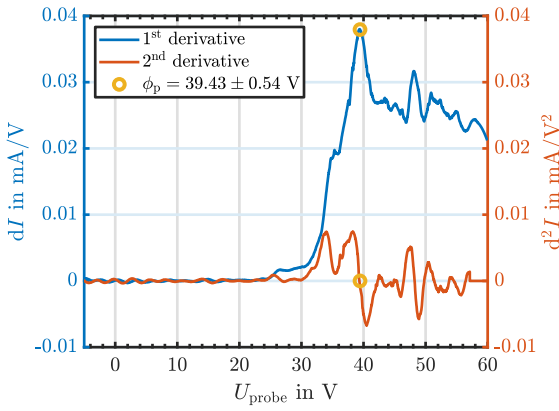


FIG. 13. Langmuir probe I-U curve with an exponential fit at the electron retardation regime (top) and first and second derivative of the probe current (bottom) measured at RUB with a signal amplitude of  $U_0 = 146$  V at 1 Pa,  $\theta = 60^{\circ}$  and a probe length of  $l_p = 5.6$  mm.

ation from the assumption of a Maxwellian distribution, as evidenced by the exponential fit of the form  $I_{\rm es} \exp(e(U_{\rm p}-\phi_{\rm p})/kT_{\rm e})$  at the electron retardation regime. Therefore, assuming a simple Maxwellian distribution is less ideal in this case. Consequently, the absolute values of the plasma parameters determined in this manner may be prone to significant errors.

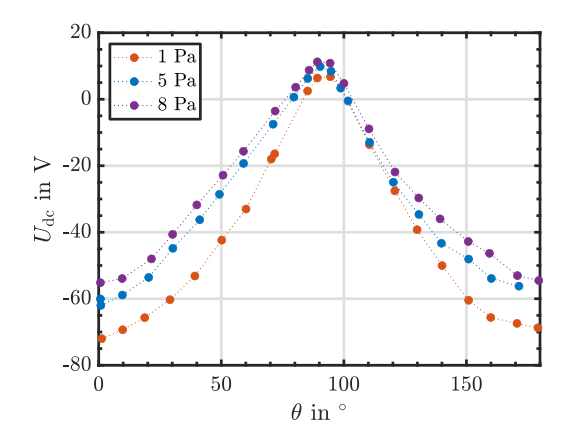


FIG. 14. Measured dc self-bias  $U_{\rm dc}$  between  $\theta=0^{\circ}$  and  $\theta=180^{\circ}$  for different pressures and  $U_0=146$  V in the 2f plasma chamber at Ruhr-University Bochum.

Nevertheless, the general trends align with those measured at CAU. The dc self-bias measured in the RUB reactor is illustrated in figure 14. Higher pressures than 8 Pa could not be examined due to the pressure measuring device used in this experiment. Compared to the dc self-bias measured in Kiel (fig. 8),  $U_{\rm dc}$  in figure 14 is shifted to less negative values and even becoming positive around  $\theta=90^{\circ}$  due to the weaker geometric asymmetry of the plasma chamber. The control range in this case is found to be close to about 53% of the applied voltage amplitude. The overall behavior of  $U_{\rm dc}$  with a changing phase angle is similar to that measured in Kiel and what one would expect.

The plasma parameters determined from the I-U curves in this discharge are presented in figure 15. Likewise, four current voltage curves per phase were recorded and averaged. In terms of absolute values, the plasma parameters determined in this setup as well as the dc self-bias show a larger control range compared to the parameters measured in Kiel (fig. 9) except for the electron density. Apart from the noisy data, the difference of the gas pressure (1 Pa in RUB and 3 Pa in CAU) also contributes to the high disparities in absolute values between RUB and CAU, as well as the different dimensions of the chambers. The profiles of the parameters at RUB exhibit a comparable pattern to the parameters in Kiel, including the pronounced increase of the electron density at  $\theta = 90^{\circ}$ . The step-like nature of the floating potential is caused by adjusting the range of the voltage ramp applied to the Langmuir probe during the measurements so that the entire I-U characteristic can be recorded. Due to this, the absolute values of  $\phi_{\rm fl}$  should be treated with caution. The small irregularity of  $\phi_D$  and  $kT_e$  at 90° as shown in the CAU results (fig. 9 b), c)) cannot be observed here, probably because of the already mentioned large errors in the evaluation of the I-U curves of the RUB data and potentially due to the smaller geometric asymmetry of the chamber. Due to the experimental setup and the placement of the window at the chamber, it was not possible to observe the light emission of the argon discharge or the sheath region by photographs. Based on the profiles of the plasma parameters, however, one would assume a similar trend of the sheath thickness as in Kiel (fig. 12).

The behavior of the parameters with a phase variation can be explained by PIC/MCC simulations.

# VI. DISCUSSION

The observed behavior of the electron density and temperature with a shifting phase angle between the harmonics can be traced back to the behavior of the electrons. Figure 16 shows the simulation results for the spatio-temporal ionization rate and the 2f signal form for different phase angles. The coordinate  $d_{\rm el}$  refers to the distance from the lower electrode. The position of the powered electrode is at  $d_{\rm el} = 75$  mm. Since the applied voltage waveform changes with  $\theta$ , the sheath dynamics and, consequently, also the excitation or ionization dynamics change as a function of  $\theta$  as well<sup>14</sup>, showing a strong ionization source at the sheath edge adjacent to the powered electrode when the sheath extends further into the discharge. These dynamics are dominated by the sheath expansion, which leads to electron beams being accelerated into the discharge<sup>9</sup>. The electrons experience energy gain through their interaction with the electric fields within the sheath<sup>51</sup>. That, in turn, influences the ionization rate and, consequently, the densities and temperatures in the bulk depending on the respective phase. In a geometrically symmetric system, the ionization maxima at the powered and grounded electrode at  $\theta = 0^{\circ}$  and  $\theta = 90^{\circ}$  should be similarly strong<sup>14</sup>. This is not the case in this geometrical asymmetric discharge as can be seen in fig. 16 a), b). The dynamics at the powered electrode dominate. In these simulations, an electron beam resulting from the expansion of the sheath at the grounded electrode contributes only minimally to the overall ionization within the discharge for all  $\theta$  due to the geometric reactor asymmetry. Unlike the dc self-bias, the ionization rate shows an asymmetry around 90°, which is exemplified in fig. 16 for c)  $\theta = 60^{\circ}$ and d)  $\theta = 120^{\circ}$ , where the dc self-bias takes on similar values. The maximum intensity of the ionization rate at  $\theta = 60^{\circ}$ is higher than at  $\theta = 120^{\circ}$ . This is probably due to the fact that at 60° the change of the voltage drop across the sheath of the powered electrode, when the sheath expands from being almost fully collapsed to its full expansion, is higher than at 120°, leading to a stronger sheath expansion heating and therefore ionization rate<sup>9</sup>. This irregularity in the ionization rate is reflected in the electron density, as shown in fig. 17 a). Here, the time-averaged ionization rate is plotted along with the electron density determined in the center of the discharge as a function of the phase angle. The same trend can be observed in the experimental data taken at RUB (fig. 15 d)) and CAU (fig. 9 d)). Looking at the order of magnitude, the simulated electron density agrees well with the experimental data at RUB. In the simulation, the electron temperature shows an inverse behavior to the density (fig. 17 b)) as one would expect and what the experimental data from CAU Kiel (fig. 9 c), d)) also reveal. However, the measurements at CAU show a dip in the electron temperature at  $90^{\circ}$ , where the density is highly increased, whereas the simulation for RUB does not show this

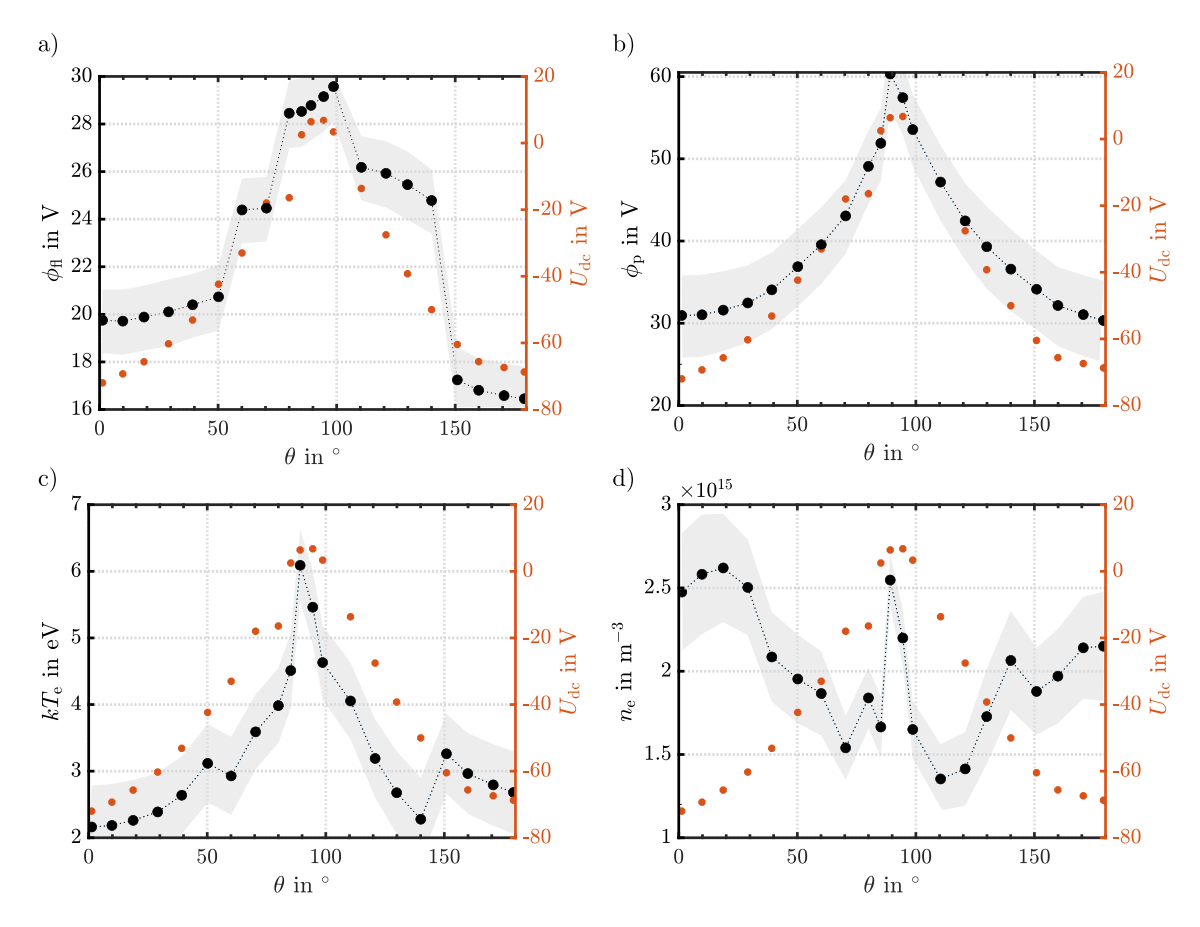


FIG. 15. a) Floating potential  $\phi_f$ , b) plasma potential  $\phi_p$ , c) electron temperature  $kT_e$  and d) electron density  $n_e$  together with  $U_{dc}$  at 1 Pa and  $U_0 = 146$  V. The plasma parameters were measured right at the center between the upper and lower electrode with a probe length of  $l_p = 5.6$  mm at Ruhr University Bochum (fig. 5). The error margins are indicated in grey.

behavior. Around this phase, the temperature is following the density. The presence of substantial errors in evaluating the I-U curves of the RUB data hinders a clear resolution of the electron temperature behavior around 90°, as observed in both the simulation and the CAU Kiel experiments. Because of this, a generally higher electron temperature is measured in the experiment (fig. 15 c)) than in the simulation (fig. 17 a)). In the simulation, the ionization rate, electron density and temperature (fig. 17 a), b)) show a slight increase at  $\theta = 90^{\circ}$ . This can be attributed to the number of sheath collapses at the powered electrode, which changes from one to two per fundamental rf period around 90°. The enhanced electron losses to the powered electrode in the presence of two sheath collapses result in an increase of the electron temperature and, thus, floating potential at 90° to ensure flux balance of electrons and ions as observed experimentally in fig. 9 a) and fig. 15 a). This causes the electron density to increase as well. The fact that this effect is observed only at  $90^{\circ}$ , but not at  $0^{\circ}$ at the grounded electrode, is a consequence of the geometric reactor asymmetry. To comprehensively characterize such a discharge, it is therefore mandatory to measure the phase dependence of the plasma parameters for the complete phase range from  $0^{\circ}$  to  $180^{\circ}$ .

The behavior of the plasma potential is also determined by

the dc self-bias. As the phase increases, the absolute value of the dc self-bias decreases, while the plasma potential 19 increases as shown in the experimental data in fig. 9 b) and 15 b), as well as in the simulation in fig. 17 c). The plasma potential is defined as the positive maximum of the time dependent potential in the plasma bulk<sup>52,53</sup>. With increasing  $|U_{dc}|$ , this becomes smaller. The discharge at CAU is strongly geometrically asymmetric, which causes a high negative dc selfbias but small plasma potential and, based on that, a small control range of  $\phi_{\rm p}$  with a shifting phase. In comparison, a less geometrically asymmetric chamber, i.e., a less negative dc self-bias, as at RUB, yields a larger plasma potential (see fig. 15 b), 17 c)). The dc self-bias calculated in the simulation (fig. 17 c)) shows the same magnitude as the experiment at RUB, except that the dc self-bias in the simulation remains negative around 90°. This is probably due to the use of simplified models describing the possible gas phase and surface processes, and neglecting secondary phenomena such as gas heating, the different materials of the facing electrodes, and the role of metastable atoms. The difference of the variation range among the plasma parameters between the experiment and simulation - e.g.,  $n_e$  varies by a factor of nearly two in figure 15 d), while the density fluctuates by around 20% in figure 17 a) - could potentially be attributed to similar factors,

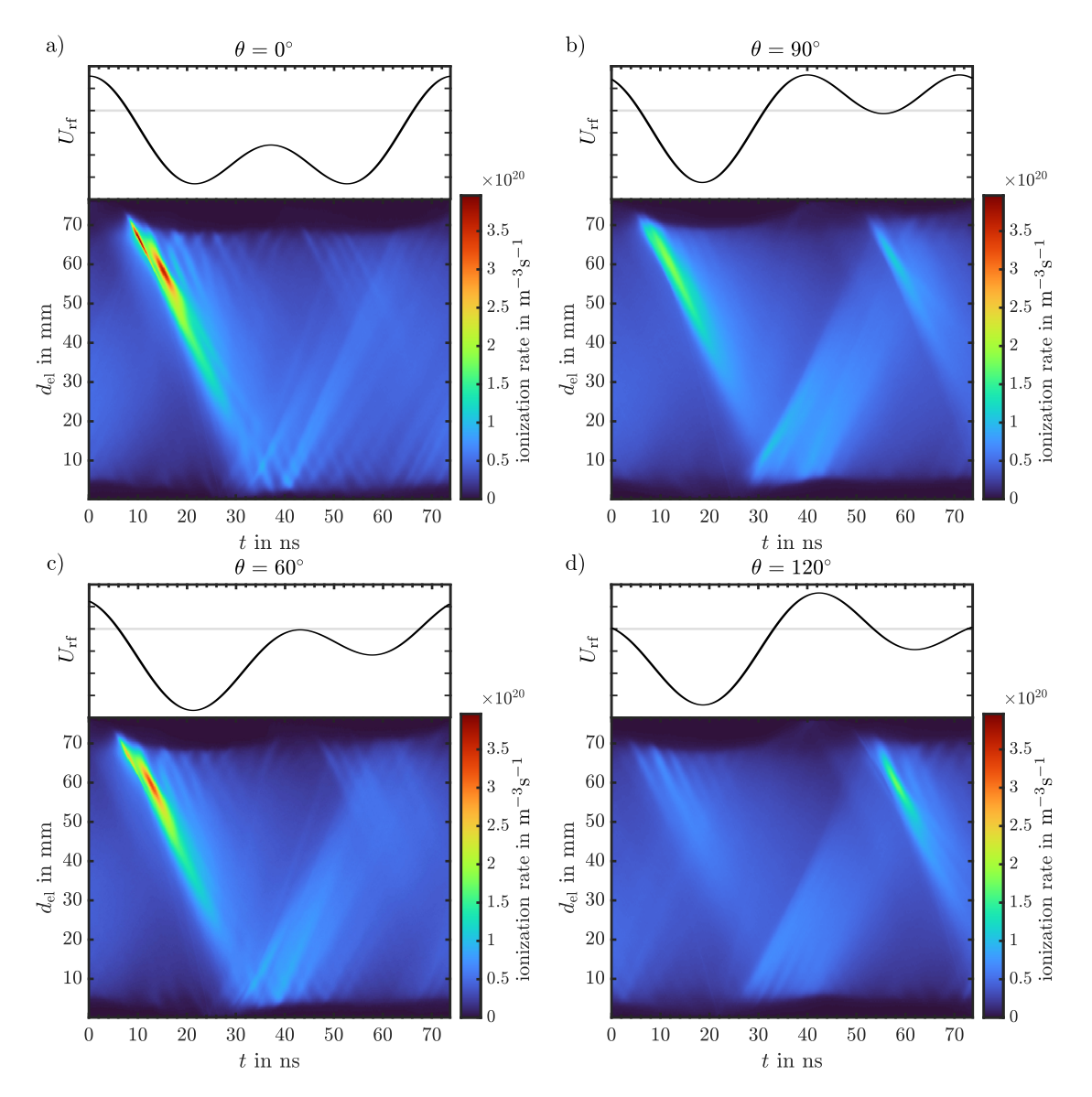


FIG. 16. Spatio-temporal distribution of the ionization rate of argon atoms resulting from PIC/MCC simulations at 1 Pa and  $U_0 = 146$  V along with the signal form within one rf cycle of the fundamental frequency for a)  $\theta = 0^{\circ}$ , b)  $\theta = 90^{\circ}$ , c)  $\theta = 60^{\circ}$  and d)  $\theta = 120^{\circ}$ . The zero line is indicated in grey.  $d_{\rm el}$  refers to the distance to the lower, grounded electrode, which is located at  $d_{\rm el} = 0$  mm and the powered electrode at  $d_{\rm el} = 75$  mm.

such as settings or missing input information within the simulation. It is also plausible that the observed variations may stem from the chosen evaluation method or, as mentioned earlier, the low signal-to-noise ratio, which complicates the evaluation process.

The simulation results reflect the general trends of the experimental data at RUB. They also show qualitatively the same evolution, e.g. of the density, with the phase angle as measured at CAU, thereby confirming the phase asymmetry.

# VII. CONCLUSION

In this study, Langmuir probe measurements in a 2f discharge have been successfully performed in two different geometric asymmetrical plasma reactors at RUB and CAU. It has been shown that a phase variation between the two harmonics influences, besides the dc self-bias, the plasma parameters, e.g. floating potential, plasma potential, electron temperature and electron density, in both experiments and enables a relatively large control range of the above mentioned parameters, while other discharge parameters, like gas pressure, stay constant. The general behavior of the parameters can be attributed to the phase-dependent sheath expansion dynamics, which cause asymmetric electron beams to be accelerated into

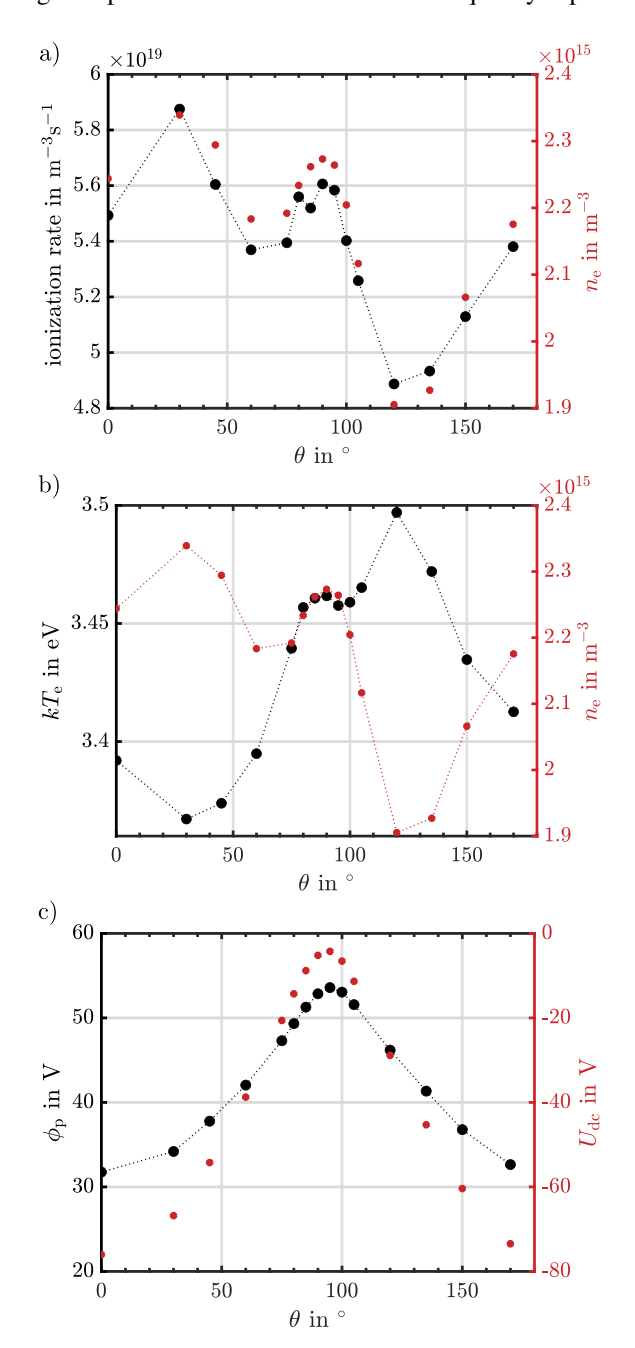


FIG. 17. Time-averaged a) ionization rate and electron density  $n_{\rm e}$ , b) electron temperature  $kT_{\rm e}$  and c) plasma potential  $\phi_{\rm p}$  including the dc self-bias  $U_{\rm dc}$  in the discharge center resulting from PIC/MCC simulations at 1 Pa and  $U_0=146$  V.

the bulk as shown by PIC/MCC simulations. The simulations qualitatively confirm the trends of the experimental data and reveal an asymmetric behavior of the ionization rate around  $\theta=90^\circ$  due to a change in the driving voltage waveform with the phase angle and the geometric asymmetry of the plasma chamber. This leads to a phase dependent and asymmetric profile of the electron temperature and density and the mean sheath thickness as it was experimentally shown. The sheath thickness was measured independently of the LP and shows

the same asymmetric behavior as the plasma parameters, confirming the credibility of the measurements. The essence of this study centers around the qualitative trends exhibited by the plasma parameters rather than their absolute values.

The simulations performed under the same experimental conditions as the RUB measurements also confirm the measured trends and magnitudes. The comparability of these trends in both experimental data and simulations justifies the basic design and handling of the Langmuir probe and implies that the observed asymmetrical behavior is a characteristic of the 2fdischarge in combination with a geometrical asymmetric reactor, where the sheath dynamics in front of the powered electrode are dominant. The differing level of geometric asymmetry between the two examined plasma chambers does not impact the existence of phase-asymmetries, but how pronounced this effect is. As long as the chamber is geometrically asymmetric, phase-asymmetries will appear in the plasma parameters. Considering these results, it is conceivable to assume that a perfectly geometrically symmetric 2f discharge would not exhibit a phase-asymmetry around 90° as it was observed with the plasma parameters. Further experimental work has to be performed to verify this statement.

### CONFLICT OF INTEREST STATEMENT

The authors have no conflicts to disclose.

# DATA AVAILABILITY STATEMENT

The data that support the findings of this study are available from the corresponding author upon reasonable request.

## **ACKNOWLEDGMENTS**

J. Schulze and I. Korolov acknowledge funding support by the German Research Foundation (DFG) in the frame of Project No. 432514770 and No. 138690629(T09) and the Collaborative Research Center SFB 1316, project A4.

P. Hartmann acknowledges the support by the National Office for Research, Development and Innovation (NKFIH) via Grant K134462.

<sup>&</sup>lt;sup>1</sup>V. M. Donnelly and A. Kornblit, Journal of Vacuum Science & Technology A 31, 050825 (2013).

<sup>&</sup>lt;sup>2</sup>A. Belkind and S. Gershman, Vac. Technol. Coat., 1–11 (2008).

<sup>&</sup>lt;sup>3</sup>S. Iwashita, T. Moriya, T. Kikuchi, M. Kagaya, N. Noro, T. Hasegawa, and A. Uedono, Journal of Vacuum Science & Technology A 36, 021515 (2018).

<sup>&</sup>lt;sup>4</sup>K. Iwata, T. Sakemi, A. Yamada, P. Fons, K. Awai, T. Yamamoto, S. Shirakata, K. Matsubara, H. Tampo, K. Sakurai, S. Ishizuka, and S. Niki, Thin Solid Films **480-481**, 199–203 (2005), eMRS 2004.

<sup>&</sup>lt;sup>5</sup>S. Matsumoto, *Electronic display devices / edited by Shoichi Matsumoto*; translated by F.R.D. Apps. (Wiley, 1990).

<sup>&</sup>lt;sup>6</sup>T. Makabe and Z. Petrovic, *Plasma Electronics: Applications in Microelectronic Device Fabrication* (CRC Press, 2006).

<sup>&</sup>lt;sup>7</sup>M. Lieberman and A. Lichtenberg, *Principles of Plasma Discharges and Materials Processing. 2nd ed.* (Hoboken N.J: Wiley-Interscience, 2005).

- <sup>8</sup>J. Schulze, E. Schüngel, and U. Czarnetzki, Journal of Physics D: Applied Physics 42, 092005 (2009).
- <sup>9</sup>B. G. Heil, U.Czarnetzki, R. P. Brinkmann, and T. Mussenbrock, Journal of Physics D: Applied Physics 41, 165202 (2008).
- <sup>10</sup>Z. Donkó, J. Schulze, B. G. Heil, and U. Czarnetzki, Journal of Physics D: Applied Physics 42, 025205 (2009).
- <sup>11</sup>Z. Donkó, J. Schulze, U. Czarnetzki, and D. Luggenhölscher, Applied Physics Letters 94, 131501 (2009).
- <sup>12</sup>J. Schulze, E. Schüngel, U. Czarnetzki, and Z. Donkó, Journal of Applied Physics **106**, 063307 (2009).
- <sup>13</sup>J. Schulze, E. Schüngel, Z. Donkó, and U. Czarnetzki, Journal of Physics D: Applied Physics 43, 225201 (2010).
- <sup>14</sup>J. Schulze, E. Schüngel, Z. Donkó, and U. Czarnetzki, Plasma Sources Science and Technology 19, 045028 (2010).
- <sup>15</sup>J. Schulze, E. Schüngel, Z. Donkó, and U. Czarnetzki, Plasma Sources Science and Technology 20, 015017 (2011).
- <sup>16</sup>J. Schulze, E. Schüngel, U. Czarnetzki, M. Gebhardt, R. P. Brinkmann, and T. Mussenbrock, Applied Physics Letters 98, 031501 (2011).
- <sup>17</sup>E. Schüngel, J. Schulze, Z. Donkó, and U. Czarnetzki, Physics of Plasmas 18, 013503 (2011).
- <sup>18</sup>U. Czarnetzki, J. Schulze, E. Schüngel, and Z. Donkó, Plasma Sources Science and Technology 20, 024010 (2011).
- <sup>19</sup>E. Schüngel, Q.-Z. Zhang, S. Iwashita, J. Schulze, L.-J. Hou, Y.-N. Wang, and U. Czarnetzki, Journal of Physics D: Applied Physics 44, 285205 (2011)
- <sup>20</sup>K. Arshad and S. Poedts, Physics of Plasmas **27**, 122904 (2020).
- <sup>21</sup>K. Arshad, "Application of kinetic theory to study twisted modes in non-maxwellian plasma," (2018).
- <sup>22</sup>E. Schüngel, D. Eremin, J. Schulze, T. Mussenbrock, and U. Czarnetzki, Journal of Applied Physics 112, 053302 (2012).
- <sup>23</sup> S. Ries, L. Banko, M. Hans, D. Primetzhofer, J. M. Schneider, A. Ludwig, P. Awakowicz, and J. Schulze, Plasma Sources Science and Technology 28, 114001 (2019).
- <sup>24</sup>J. Schulze, A. Derzsi, and Z. Donkó, Plasma Sources Science and Technology 20, 045008 (2011).
- <sup>25</sup>S. Bienholz, T. Styrnoll, and P. Awakowicz, Journal of Physics D: Applied Physics 47, 065201 (2014).
- <sup>26</sup>J. Schulze, E. Schüngel, Z. Donkó, D. Luggenhölscher, and U. Czarnetzki, Journal of Physics D: Applied Physics 43, 24016 (2010).
- <sup>27</sup>V. Schneider and H. Kersten, Review of Scientific Instruments 89, 103505 (2018).

- <sup>28</sup>J. Schleitzer, V. Schneider, and H. Kersten, Physics of Plasmas 28, 083506 (2021).
- <sup>29</sup>J. Benedikt, H. Kersten, and A. Piel, Plasma Sources Science and Technology 30, 033001 (2021).
- <sup>30</sup>Z. Donkó, A. Derzsi, M. Vass, B. Horváth, S. Wilczek, B. Hartmann, and P. Hartmann, Plasma Sources Science and Technology 30, 095017 (2021).
- <sup>31</sup>H. M. Mott-Smith and I. Langmuir, Phys. Rev. **28**, 727–763 (1926).
- <sup>32</sup>A. Piel, Plasma Physics, An Introduction to Laboratory, Space and Fusion Plasmas, 1st ed. (Springer-Verlag, 2010).
- <sup>33</sup>J. E. Allen, Physica Scripta **45**, 497 (1992).
- <sup>34</sup>I. H. Hutchinson, *Principles of Plasma Diagnostics*, 2nd ed. (Cambridge University Press, 2002).
- <sup>35</sup>R. L. Merlino, American Journal of Physics **75**, 1078–1085 (2007).
- <sup>36</sup>A. Wendt, Review of Scientific Instruments **72**, 2926–2930 (2001).
- <sup>37</sup>P. Chatterton, J. Rees, W. Wu, and K. AL-Assadi, Vacuum **42**, 489–493 (1991).
- <sup>38</sup>A. Cantin and R. R. J. Gagné, Applied Physics Letters **30**, 316–319 (1977).
- <sup>39</sup>A. Piel, Plasma Physics: An introduction to Laboratory, Space, and Fusion Plasmas, 2nd ed. (Springer International Publishing AG, 2017).
- <sup>40</sup>V. A. Godyak, R. B. Piejak, and B. M. Alexandrovich, Plasma Sources Science and Technology 1, 36 (1992).
- <sup>41</sup>A. V. Phelps and Z. L. Petrovic, Plasma Sources Science and Technology 8, R21 (1999).
- <sup>42</sup>A. V. Phelps, Journal of Applied Physics **76**, 747–753 (1994).
- <sup>43</sup>S. Mittal, International Journal of High Performance Computing and Networking 7, 292–298 (2014).
- <sup>44</sup>M. Vass, P. Palla, and P. Hartmann, Plasma Sources Science and Technology 31, 064001 (2022).
- <sup>45</sup>L. Wang, P. Hartmann, Z. Donkó, Y.-H. Song, and J. Schulze, Plasma Sources Science and Technology 30, 085011 (2021).
- <sup>46</sup>Z. Juhasz, J. Durian, A. Derzsi, S. Matejčík, Z. Donkó, and P. Hartmann, Computer Physics Communications 263, 107913 (2021).
- <sup>47</sup>C. Böhm and J. Perrin, Review of Scientific Instruments **64**, 31–44 (1993).
- <sup>48</sup>M. Hopkins, Journal of Research of the National Institute of Standards and Technology **100**, 415 (1996).
- <sup>49</sup>B. Bora and L. Soto, Journal of Physics: Conference Series **591**, 012064 (2015).
- <sup>50</sup>F. Su, W. Wang, A. G. Burns, X. Yue, and F. Zhu, Journal of Geophysical Research: Space Physics **120**, 10,724–10,739 (2015).
- <sup>51</sup>B. G. Heil, J. Schulze, T. Mussenbrock, R. P. Brinkmann, and U. Czarnetzki, IEEE Transactions on Plasma Science 36, 1404–1405 (2008).
- <sup>52</sup>K. Köhler, J. W. Coburn, D. E. Horne, E. Kay, and J. H. Keller, Journal of Applied Physics **57**, 59–66 (1985).
- <sup>53</sup>J. W. Coburn and E. Kay, Journal of Applied Physics **43**, 4965–4971 (1972).